Available online at www.sciencedirect.com
SCIENCE DIRECT®
Journal of Computational Physics 210 (2005) 32–54
JOURNAL OF COMPUTATIONAL PHYSICS
www.elsevier.com/locate/jcp

Sharp interface Cartesian grid method II: A technique for simulating droplet interactions with surfaces of arbitrary shape

H. Liu, S. Krishnan, S. Marella, H.S. Udaykumar *

Department of Mechanical and Industrial Engineering, University of Iowa, Iowa City, IA-52246, United States

Received 1 July 2004; received in revised form 8 March 2005; accepted 17 March 2005
Available online 26 May 2005

Abstract

A fixed-grid, sharp interface method is developed to simulate droplet impact and spreading on surfaces of arbitrary shape. A finite-difference technique is used to discretize the incompressible Navier–Stokes equations on a Cartesian grid. To compute flow around embedded solid boundaries, a previously developed sharp interface method for solid immersed boundaries is used. The ghost fluid method (GFM) is used for fluid–fluid interfaces. The model accounts for the effects of discontinuities such as density and viscosity jumps and singular sources such as surface tension in both bubble and droplet simulations. With a level-set representation of the propagating interface, large deformations of the boundary can be handled easily. The model successfully captures the essential features of interactions between fluid–fluid and solid–fluid phases during impact and spreading. Moving contact lines are modeled with contact angle hysteresis and contact line motion on non-planar surfaces is computed. Experimental observations and other simulation results are used to validate the calculations.

Keywords: Multiphase flow; Sharp interface method; Cartesian grid; Level-sets; Droplet impact

1. Introduction

In Part I [18] an easily implemented three-dimensional sharp interface treatment was developed for solid–fluid boundaries immersed in flows. The method relied on a framework that meshes well with the sharp-interface ghost fluid method (GFM) [4,12,16] for fluid–fluid boundaries. In this paper, the sharp-interface treatment of the solid–fluid boundaries is combined with the GFM to simulate interactions between

* Corresponding author. Tel.: +1 319 384 0832; fax: +1 319 335 5669.
E-mail address: ush@engineering.uiowa.edu (H.S. Udaykumar).

0021-9991/$ - see front matter © 2005 Elsevier Inc. All rights reserved.
doi:10.1016/j.jcp.2005.03.032

droplets and solid surfaces. The challenge here is to treat all interfaces sharply while allowing for large interface deformations, including fragmentation, and to handle moving contact line dynamics. Treatment of contact line conditions is fairly challenging with the level-set method when compared to say the VOF method [2] or Lagrangian finite element methods [5]. In the VOF approach the contact angle can be imposed by reconstructing the partial volume in the fluid–fluid interface cell that lies adjacent to the solid surface such that the reconstructed surface (typically a plane) assumes the specified contact angle with respect to the solid surface [2]. In the Lagrangian moving mesh approach the mesh node that lies on the solid surface can be moved to apply the desired angle [5]. For junctions between multiple fluid phases several techniques [26,32] have been investigated in the level-set framework. For solid–fluid–fluid tri-junctions, Sussman [27] has presented a technique for applying contact angles. An alternative approach based on a local level-set reconstruction was outlined by Noble et al. [20]. This second approach has been modified and advanced in the present work; it was found to be more suitable for situations such as droplet impact, where the contact angle evolves from the pre-impact to the spreading and equilibrium resting situations. Additionally, the method is designed to enable simulations of droplet spreading on arbitrarily shaped solid surfaces.

2. Methods for simulation of droplet impact

Harlow and Shannon [9] were the first to simulate droplet impact on a solid surface. A "marker-and-cell" (MAC) finite-difference method was used to solve the NS equations. To simplify the problem, viscosity and surface tension were neglected so that a physically accurate representation was obtained only for the very initial inertia-dominated stages after impact. Later workers [30] improved the MAC model of Harlow and Shannon to include surface tension and viscosity effects.

The volume-of-fluid (VOF) method has been used frequently in studying droplet-wall interactions. Trapaga and coworkers [28,29] applied a commercial code FLOW-3D, using VOF tracking, to study isothermal impingement of liquid droplets in a thermal spray process. Liu et al. [17] used a VOF-based code, RIPPLE [14] to study the impact of a molten metal droplet and its subsequent solidification. Pasandideh-Fard et al. [22] have shown that the values of contact angle can significantly influence model predictions in combined experimental and numerical studies of droplet impact. The VOF method has also been applied to simulate droplet spreading by Renardy et al. [24] for droplets in prior contact with a wall.

Lagrangian finite-element methods were used by Fukai et al. [5–7] to model droplet impact normal to a flat plate. Like most previous researchers, experimentally measured contact angles were used as inputs to their previous numerical model. With the inclusion of contact angle dynamics, their model reproduced experimental data, not only in the spreading phase but also during recoil and oscillation. Baer et al. [1] used a simple but computationally tractable linear variation between contact line velocity and contact angle in their 3D simulations. They successfully captured contact angle hysteresis and critical contact angles.

The level-set method was used in combination with a curvilinear grid finite-volume approach by Zheng and Zhang [33] to study droplet spreading and solidification. However, they did not compare their predictions of droplet shapes during impact with experimental or numerical results. Recently the phase field method, has also been applied to simulations of wetting and spreading of droplets on surfaces [11].

Three-dimensional simulations of droplet impact have only been possible in recent years. Bussmann et al. [2] demonstrated a three-dimensional, finite difference, fixed-grid Eulerian model using VOF tracking. Droplet impact and spreading on surfaces of arbitrary shape has also received limited theoretical treatment in the literature [23]. Droplet impact on an inclined plane and on a step was simulated in [2]. Although their model for the variation of contact angle with velocity was simplified, the 3D model yielded good predictions of gross fluid deformation during droplet impact onto an incline and onto an edge.

In the following sections a sharp-interface method is described for the simulation of droplet/ bubble interactions with arbitrary solid interfaces. The method relies on level-set representations of all interfaces

and provides the capability to follow the dynamics of contact lines. The results are compared with experimental as well as numerical results.

3. The current method

3.1. Equations to be solved

3.1.1. Governing equations

The equations to be solved for viscous incompressible flow are

Continuity equation:

$$\nabla \cdot \vec{u} = 0, \tag{1}$$

Momentum equation:

$$\frac{\partial \vec{u}}{\partial t} + \vec{u} \cdot \nabla \vec{u} = -\frac{1}{\rho}\nabla p + v\nabla^2 \vec{u} + \vec{g}, \tag{2}$$

where t is time and $\vec{g}$ is the gravitational acceleration. The velocity vector is $\vec{u} = \langle u, v, w \rangle$ in three-dimensions, pressure is denoted by p and viscosity by v. In the present work, we solve the above equations in two-dimensional planar as well as axisymmetric situations.

3.1.2. Interface conditions

For a solid–fluid boundary, a no-slip condition is applied everywhere except in the immediate vicinity of the moving contact line where a slip boundary condition is applied. A Neumann condition is applied for the pressure at the interface [31].

At a fluid–fluid interface, such as illustrated in Fig. 1, the following jump conditions (specialized here into the 2D vector form) apply [12]:

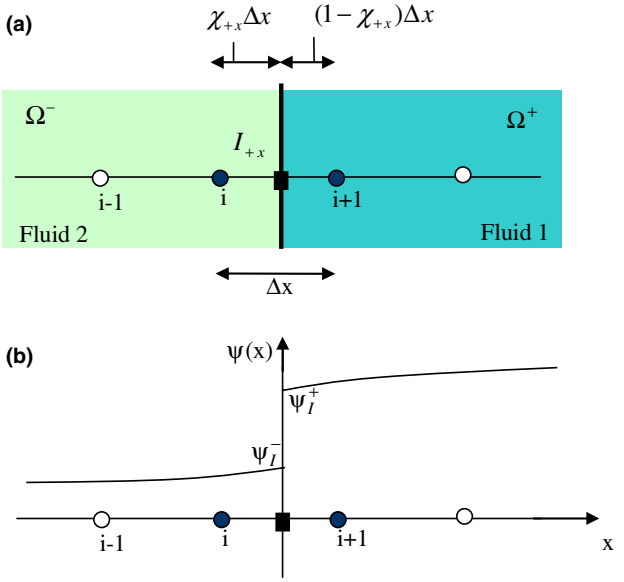

Fig. 1. 1D illustration of a sharp fluid–fluid interface lying between two grid points i and $i+1$. The variation of a field ψ is shown along with the jump conditions that apply on the interface.

$$[\vec{u}] = 0, \tag{3}$$

$$\begin{pmatrix} [u_x] & [u_y] \\ [v_x] & [v_y] \end{pmatrix} = -\frac{[\mu]}{\hat{\mu}} \begin{pmatrix} \vec{n} \\ \vec{t} \end{pmatrix}^{\mathrm{T}} \begin{pmatrix} 0 & 0 \\ \hat{\alpha} & 0 \end{pmatrix} \begin{pmatrix} \vec{n} \\ \vec{t} \end{pmatrix}, \tag{4}$$

$$[p] - 2[\mu](\nabla u \cdot \vec{n}, \nabla v \cdot \vec{n}) \cdot \vec{n} = \sigma\kappa, \tag{5}$$

$$\left[\frac{\nabla p}{\rho}\right] = \left[\frac{\mu(\nabla^2 \vec{u})}{\rho}\right]. \tag{6}$$

In the above equations, the square braces indicate jumps in the quantity across the interface, i.e. $[\psi] = \psi_{\mathrm{I}}^{+} - \psi_{\mathrm{I}}^{-}$, subscript "I" indicates the interfacial value and the normal at the interface points from the Ω^{-} to Ω^{+} side. $\vec{n}$ and $\vec{t}$ are the normal and tangent to the interface, respectively. In the above:

$$\hat{\alpha} = \frac{\alpha^{-}\alpha^{+}}{(\alpha^{+}\chi + \alpha^{-}(1-\chi))} \quad \text{and} \quad \hat{\mu} = \frac{\mu^{-}\mu^{+}}{(\mu^{+}\chi + \mu^{-}(1-\chi))}, \tag{7}$$

where

$$\alpha = (\nabla u \cdot \vec{n}, \nabla v \cdot \vec{n}) \cdot \vec{t} + (\nabla u \cdot \vec{t}, \nabla v \cdot \vec{t}) \cdot \vec{n}. \tag{8}$$

As illustrated in Fig. 1 the level-set information (ϕ_1 field for the first immersed interface) can be used [18] to obtain

$$\chi = \frac{\Delta x_{\mathrm{I}}}{\Delta x} \cong \frac{|0 - (\phi_l)_{i,j}|}{|(\phi_l)_{i+1,j} - (\phi_l)_{i,j}|}. \tag{9}$$

3.2. Flow solver

The flow solver is described in detail in [18]. A cell-centered collocated arrangement of the flow variables is used to discretize the governing equations. A two-step fractional step method [31] is used to advance the solution in time. A standard level-set evolution equation is used to move the interfaces. For the grid points away from both fluid–fluid and solid–fluid interfaces, the convection term and pressure gradient can be computed to second-order accuracy using central differences, which yields a 5-point stencil for discretization in 2D and results in a symmetric pentadiagonal banded matrix of coefficients. The sharp interface approach presented in [18] is used to develop discretizations for the interfacial nodes adjacent to a solid–fluid interface. However, discretization in a sharp fashion for interfacial nodes needs to be performed with care when both interfaces (fluid–fluid and solid–fluid) coexist, as can happen during impact and spreading.

For interfacial points (grid points that satisfy the criterion $(\phi_l)_{i,j}(\phi_l)_{\mathrm{nb}} \leqslant 0$, where "nb" denotes an immediate neighbor along the coordinate directions), the possible situations can be categorized according to the locations of the interfaces in the computational domain as illustrated in Fig. 2. In the case of a sharp solid–fluid interface, such as shown in Fig. 2(a) the discretization is given in [18]. When a fluid–fluid interface is present, the jump conditions make their appearance in the discrete form of the Laplace operator ($\nabla \cdot \beta \nabla \psi$), i.e. in the viscous terms in the momentum equation and in the pressure Poisson equation. For the case shown in Fig. 2(b) the discretization that includes jump conditions (Eqs. (3)–(6)) is developed according to the ghost fluid method [12]. For the case in Fig. 2(c) the discretization needs to be carefully handled since both the solid–fluid interface conditions and the fluid–fluid interface conditions need to be brought into the discrete operators. For the case in Fig. 2(d) the Fluid 1 layer is below the resolution afforded by the mesh.

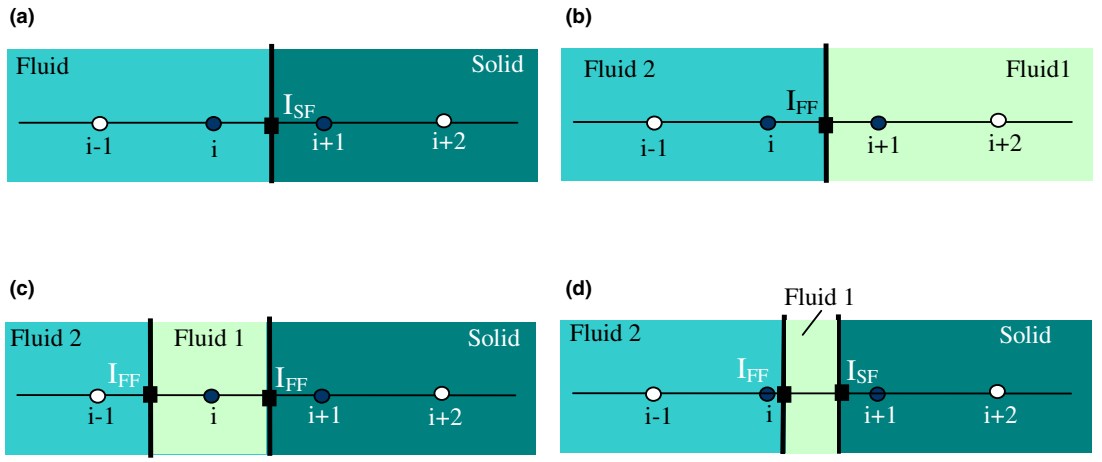

Fig. 2. Illustration of the different situations that can arise in the fixed grid capture of interacting fluid–fluid and solid–fluid interfaces. (a) An isolated solid–fluid interface. (b) An isolated fluid–fluid interface. (c) A fluid–fluid interface lying adjacent to a solid–fluid interface with a grid point lying in the intervening region. (d) A fluid–fluid interface and solid–fluid interface in contact.

In this case the liquid–gas interface is ignored and the discretization then reverts back to that for the solid–liquid interface in Fig. 2(a).

We will now present a discrete representation of the case in Fig. 2(b) that is drawn from the standard GFM approach but cast in a form that is compatible with the discrete form for the solid–fluid interfaces presented in [18]. Then, the discretization procedure for the case in Fig. 2(c) will be presented. For simplicity the discretization is shown for a one-dimensional case (x-direction) only. The discretization for higher dimensions proceeds in similar fashion independently in each coordinate direction.

3.3. A general form of the discretization for the operators

The jump conditions at the fluid–fluid interfaces manifest themselves primarily in the form $(\beta\psi_x)_x$. These arise in the viscous terms in the momentum equation (where $\beta = \nu$) and the pressure Poisson equation (where $\beta = \frac{1}{\rho}$). Consider the picture in Fig. 2(b). The discretization of the Poisson-type term in the x-direction proceeds as follows:

$$(\beta\psi_x)_x = \frac{\left(\beta\frac{\partial\psi}{\partial x}\right)_{i+1/2j} - \left(\beta\frac{\partial\psi}{\partial x}\right)_{i-1/2j}}{\Delta x}. \tag{10}$$

3.3.1. Case 2 (Fig. 2(b))

If the fluid–fluid interface lies between points (i, j) and $(i + 1, j)$ as shown in Fig. 1(a) and the jump conditions at the interface are [12]:

$$[\psi] = a_{\mathrm{I}_{+x}} = \psi^{+}_{\mathrm{I}_{+x}} - \psi^{-}_{\mathrm{I}_{+x}}, \tag{11}$$

$$[\beta\psi_x] = b_{\mathrm{I}_{+x}} = (\beta\psi_x)^{+}_{\mathrm{I}_{+x}} - (\beta\psi_x)^{-}_{\mathrm{I}_{+x}}. \tag{12}$$

In discrete form, following the GFM approach [12] the second jump condition can be written as

$$\beta^{+}\left(\frac{\psi_{i+1,j} - \psi^{+}_{\mathrm{I}_{+x}}}{(1-\chi)\Delta x}\right) - \beta^{-}\left(\frac{\psi^{-}_{\mathrm{I}_{+x}} - \psi_{i,j}}{\chi\Delta x}\right) = b_{\mathrm{I}_{+x}}, \tag{13}$$

where χ is given by Eq. (9). This involves a first-order estimate of the gradients on each side of the interface. In fact the GFM [12] approach is identical to the IIM [15] if the Taylor expansions in IIM are carried to first-order only and the second-derivative jumps are ignored.

Using the first jump condition in Eq. (11):

$$\beta^+\left(\frac{\psi_{i+1,j}-\psi^-_{\mathrm{I}_{+x}}-a_{\mathrm{I}_{+x}}}{(1-\chi)\Delta x}\right)-\beta^-\left(\frac{\psi^-_{\mathrm{I}_{+x}}-\psi_{i,j}}{\chi\Delta x}\right)=b_{\mathrm{I}_{+x}}. \tag{14}$$

This gives

$$\psi^-_{\mathrm{I}_{+x}}=\frac{\beta^+\chi}{(\beta^+\chi+\beta^-(1-\chi))}\psi_{i+1,j}+\frac{\beta^-(1-\chi)}{(\beta^+\chi+\beta^-(1-\chi))}\psi_{i,j}-\frac{\beta^+\chi}{(\beta^+\chi+\beta^-(1-\chi))}a_{\mathrm{I}_{+x}}-\frac{(1-\chi)\chi\Delta x}{(\beta^+\chi+\beta^-(1-\chi))}b_{\mathrm{I}_{+x}}. \tag{15}$$

Therefore, using this interfacial value in Eq. (10) one obtains

$$(\beta\psi_x)_x=\frac{\hat\beta}{\Delta x^2}(\psi_{i+1,j}-\psi_{i,j})-\frac{\beta^-}{\Delta x^2}(\psi_{i,j}-\psi_{i-1,j})-\frac{\hat\beta}{\Delta x^2}a_{\mathrm{I}_{+x}}-\frac{(1-\chi)}{\Delta x}\frac{\hat\beta}{\beta^+}b_{\mathrm{I}_{+x}}, \tag{16}$$

where

$$\hat\beta=\frac{\beta^+\beta^-}{(\beta^+\chi+\beta^-(1-\chi))}. \tag{17}$$

Similarly, the expression for the case where the interface lies between points (i,j) and $(i-1,j)$ can also be obtained.

3.3.2. Case 3 (Fig. 2(c))

In this case the discretization at point (i,j) has to account for the presence of the solid–fluid boundary (represented by level-set field ϕ_{l_1}) between point (i,j) and $(i+1,j)$ and the fluid–fluid boundary (represented by level-set field ϕ_{l_2}) between point (i,j) and $(i-1,j)$. Details of this case are shown in Fig. 3. Define

$$\chi_{+x}=\frac{|(\phi_{l_1})_{i,j}|}{|(\phi_{l_1})_{i,j}|+|(\phi_{l_1})_{i+1,j}|},\qquad \chi_{-x}=\frac{|(\phi_{l_2})_{i,j}|}{|(\phi_{l_2})_{i,j}|+|(\phi_{l_2})_{i-1,j}|}. \tag{18}$$

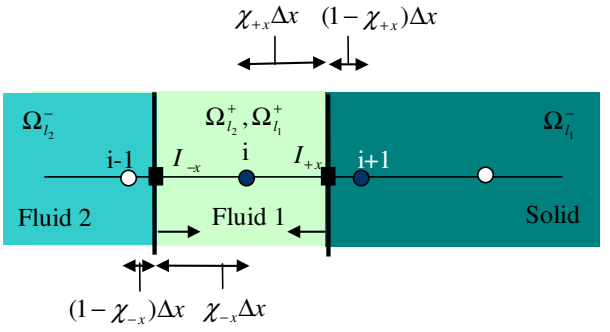

Fig. 3. Detail of the one-dimensional specialization of interfacial points when a fluid–fluid interface and solid–fluid interface interact. Point i lies between a solid–fluid and a fluid–fluid interface at the instant before contact.

A first-order estimate is computed from:

$$(\beta\psi_x)_x = \frac{\beta_{i,j}\left(\frac{\psi^+_{\mathrm{I}_{+x}} - \psi_{i,j}}{\chi_{+x}\Delta x}\right) - \beta_{i,j}\left(\frac{\psi_{i,j} - \psi^+_{\mathrm{I}_{-x}}}{\chi_{-x}\Delta x}\right)}{\left(\chi_{+x} + \frac{1}{2}\right)\Delta x}. \tag{19}$$

Using the jump conditions at the liquid–gas interface:

$$\psi^+_{\mathrm{I}_{-x}} - \psi^-_{\mathrm{I}_{-x}} = a_{\mathrm{I}_{-x}}, \tag{20}$$

$$(\beta\psi_x)^+_{\mathrm{I}_{-x}} - (\beta\psi_x)^-_{\mathrm{I}_{-x}} = b_{\mathrm{I}_{-x}} = \beta^+\frac{(\psi_{i,j} - \psi^+_{\mathrm{I}_{-x}})}{\chi_{-x}\Delta x} - \beta^-\frac{(\psi^-_{\mathrm{I}_{-x}} - \psi_{i-1,j})}{(1-\chi_{-x})\Delta x}. \tag{21}$$

From the above two expressions one obtains

$$\begin{aligned}\psi^+_{\mathrm{I}_{-x}} = {} & \frac{\beta^-\chi_{-x}}{(\beta^-\chi_{-x} + \beta^+(1-\chi_{-x}))}\psi_{i-1,j} + \frac{\beta^-(1-\chi_{-x})}{(\beta^-\chi_{-x} + \beta^+(1-\chi_{-x}))}\psi_{i,j} - \frac{\beta^-\chi_{-x}}{(\beta^-\chi_{-x} + \beta^+(1-\chi_{-x}))}a_{\mathrm{I}_{-x}} \\ & - \frac{(1-\chi_{-x})\chi_{-x}\Delta x}{(\beta^-\chi_{-x} + \beta^+(1-\chi_{-x}))}b_{\mathrm{I}_{-x}}.\end{aligned} \tag{22}$$

Therefore, substituting in Eq. (19) and simplifying we get

$$(\beta\psi_x)_x = \frac{\beta^+}{\chi_{+x}(\chi_{+x}+\frac{1}{2})\Delta x^2}(\psi^+_{\mathrm{I}_{+x}} - \psi_{i,j}) - \frac{\hat\beta_{-x}}{(\chi_{+x}+\frac{1}{2})\Delta x^2}(\psi_{i,j} - \psi_{i-1,j}) + \frac{\hat\beta_{-x}}{(\chi_{+x}+\frac{1}{2})\Delta x^2}a_{\mathrm{I}_{-x}} - \frac{\hat\beta_{-x}}{\beta^-}\frac{\Delta x(1-\chi_{-x})}{(\chi_{+x}+\frac{1}{2})\Delta x^2}b_{\mathrm{I}_{-x}}, \tag{23}$$

where

$$\hat\beta_{-x} = \frac{\beta^-\beta^+}{(\beta^-\chi_{-x} + \beta^+(1-\chi_{-x}))}. \tag{24}$$

For the situation where the liquid–gas interface lies on the right and the solid–liquid interface lies to the left a similar expression can be obtained.

3.3.3. The general expression

The situation in Fig. 3 can be considered to be the most general case, encompassing all the cases shown in Fig. 2(a)–(d). Therefore, based on the expressions obtained for the above two cases and those provided in [18] for Case 1 (Fig. 2(a)), and considering that Case 4 corresponds to Case 1 (when the unresolved sliver of the Fluid 1 phase is ignored), a general discrete form for $(\beta\psi_x)_x$ can be obtained. The following expressions apply where multiple (say $L_{\max}$) embedded boundaries are present in the flow:

$$\begin{aligned}(\beta\psi_x)_x = {} & \hat\beta_{+x}\alpha_{+x}\frac{(\psi_{+x} - \psi_{i,j})}{\gamma_x\Delta x^2} - \hat\beta_{-x}\alpha_{-x}\frac{(\psi_{i,j} - \psi_{-x})}{\gamma_x\Delta x^2} + \frac{\hat\beta_{+x}a_{+x}}{\gamma_x\Delta x^2} + \frac{\hat\beta_{-x}a_{-x}}{\gamma_x\Delta x^2} + \frac{\hat\beta_{+x}(1-\chi_{+x})b_{+x}}{\beta_{i+1}\gamma_x\Delta x^2} \\ & + \frac{\hat\beta_{-x}(1-\chi_{-x})b_{-x}}{\beta_{i-1}\gamma_x\Delta x^2},\end{aligned} \tag{25a}$$

where the coefficients $\hat\beta_{\pm x}$, $\alpha_{\pm x}$ and γ_x are obtained as follows:

$$(s_l)_{\pm x} = \left\{\frac{(\phi_l)_{i,j}(\phi_l)_{i\pm1,j}}{|(\phi_l)_{i,j}(\phi_l)_{i\pm1,j}|}\right\}, \qquad s_{\pm x} = \min_{l=1,L_{\max}}\{(s_l)_{\pm x}\}, \tag{25b}$$

$$\chi_{\pm x} = \min_{l=1,L_{\max}} \left\{ |\max((s_l)_{\pm x}, 0)| + \frac{|(\phi_l)_{i,j}|}{|(\phi_l)_{i,j}| + |(\phi_l)_{i\pm1,j}|} |\min((s_l)_{\pm x}, 0)| \right\}, \tag{25c}$$

$$\delta_{\pm x} = \begin{cases} 1 & \text{if solid–fluid interface between } (i,j) \text{ and } (i \pm 1, j), \\ 0 & \text{otherwise,} \end{cases} \tag{25d}$$

$$\psi_{\pm x} = \delta_{\pm x}\psi_{\mathrm{I}_{\pm x}} + (1 - \delta_{\pm x})\psi_{i\pm1,j}, \tag{25e}$$

$$\alpha_{\pm x} = \delta_{\pm x}\frac{1}{\chi_{\pm x}} + (1 - \delta_{\pm x}), \tag{25f}$$

$$\hat{\beta}_{\pm x} = \frac{\beta_{i,j}\beta_{i\pm1,j}}{\beta_{i,j}\chi_{\pm x} + \beta_{i\pm1,j}(1 - \chi_{\pm x})}, \tag{25g}$$

$$\gamma_x = \delta_{+x}\frac{\chi_{+x}}{2} + \delta_{-x}\frac{\chi_{-x}}{2} + (1 - \delta_{+x})\left\{\frac{1}{2} + \frac{1}{2}\chi_{-x}\delta_{-x}|\min(s_{+x}, 0)|\right\} + (1 - \delta_{-x})\left\{\frac{1}{2} + \frac{1}{2}\chi_{+x}\delta_{+x}|\min(s_{-x}, 0)|\right\} \tag{25h}$$

$$a_{\pm x} = \frac{(\phi_{l_1})_{i,j}}{|(\phi_{l_1})_{i,j}|} a_{\mathrm{I}_{\pm x}} |\min(s_{\pm x}, 0)|(1 - \delta_{\pm x}), \tag{25i}$$

$$b_{\pm x} = \pm\frac{(\phi_{l_2})_{i,j}}{|(\phi_{l_2})_{i,j}|} b_{\mathrm{I}_{\pm x}} |\min(s_{\pm x}, 0)|(1 - \delta_{\pm x}). \tag{25j}$$

The advantage of casting the equations in the above form is that implementation in a computer code is straightforward. Note that Eqs. (25) reduce, in the appropriate cases, to the discrete form for a solid–fluid interface obtained in Marella et al. (2004), to Eq. (16) for a fluid–fluid interface, and to standard central differences in the absence of interfaces. The above coefficient assembly also applies to any point in the domain, including points that lie away from the interface and interface adjacent points that conform to any of the cases shown in Fig. 2. Thus, a sharp-interface calculation that handles solid–fluid immersed boundaries, fluid–fluid immersed boundaries and their interactions can be easily programmed by a few lines of code that modify a simple uniform Cartesian grid flow solver. The discretization of the components of the Laplace operator involving derivatives in the y- and z-directions is performed with procedures identical to that presented above for the x-derivatives. The above form unifies the treatment of the sharp interface method presented in [18] with the ghost-fluid method [12], and is a first-order implementation of the immersed interface method [15]. The treatment of the convection term proceeds in a fashion identical to that described in [18].

4. Velocity correction

Once the intermediate velocity and pressure fields have been obtained as described above, the velocity correction step is performed to update to a divergence-free velocity field. For grid points that lie away from the interface this is straightforward. For points that lie next to the immersed boundary the corrections are to be performed based on the different situations that may arise at such points, as illustrated in Fig. 2. The pressure gradients required to correct the cell center and cell face velocities have to be evaluated in a manner consistent with the evaluation performed for obtaining the gradients while discretizing the Laplace

operator in the PPE. For the case shown in Fig. 2(a) the correction procedure has been provided in [18]. For the particular case illustrated in Figs. 2(b) the corrections are effected as follows:

$$u_{i,j}^{n+1} = u_{i,j}^{*} - \frac{\Delta t}{\rho_{i,j}\Delta x(\frac{1}{2}+\chi_{+x})}(p_{\mathrm{I}_{+x}}^{-} - p_{i-1/2,j}), \tag{26}$$

$$u_{i+1/2,j}^{n+1} = u_{i+1/2,j}^{*} - \frac{\Delta t}{\rho_{i+1/2,j}\Delta x\chi_{+x}}(p_{\mathrm{I}_{+x}}^{-} - p_{i,j}). \tag{27}$$

For the case in Fig. 2(c) the corrections are obtained from:

$$u_{i,j}^{n+1} = u_{i,j}^{*} - \frac{\Delta t}{\rho_{i,j}\Delta x(\chi_{-x}+\chi_{+x})}(p_{\mathrm{I}_{+x}}^{+} - p_{\mathrm{I}_{-x}}^{+}), \tag{28}$$

$$u_{i+1/2,j}^{n+1} = u_{i+1/2,j}^{*} - \frac{\Delta t}{\rho_{i+1/2,j}\Delta x\chi_{+x}}(p_{\mathrm{I}_{+x}}^{+} - p_{i,j}), \tag{29}$$

$$u_{i-1/2,j}^{n+1} = u_{i-1/2,j}^{*} - \frac{\Delta t}{\rho_{i-1/2,j}\Delta x\chi_{-x}}(p_{i,j} - p_{\mathrm{I}_{-x}}^{+}). \tag{30}$$

In the above equations, the interface pressure in case of fluid–fluid interfaces is obtained by applying the jump conditions for pressure listed in Eqs. (5) and (6). In the case of solid–fluid interfaces, the pressure is obtained by as described in [18].

A compact way of writing the corrections for all the situations is

$$u_{i,j}^{n+1} = u_{i,j}^{*} - \frac{\Delta t}{\rho_{i,j}}\frac{\alpha_x(p_{+x}-p_{-x})}{\Delta x}, \tag{31a}$$

where

$$p_{+x} = p_{i+1/2,j}|\max(s_{+x},0)| + p_{\mathrm{I}_{+x}}|\min(s_{+x},0)|, \tag{31b}$$

$$p_{-x} = p_{i-1/2,j}|\max(s_{-x},0)| + p_{\mathrm{I}_{-x}}|\min(s_{-x},0)|, \tag{31c}$$

$$\alpha_x = \frac{1}{(\chi_{+x}+\chi_{-x})}, \tag{31d}$$

$$(s_l)_{\pm x} = \left\{\frac{(\phi_l)_{i,j}(\phi_l)_{i+1,j}}{|(\phi_l)_{i,j}(\phi_l)_{i+1,j}|}\right\}, \qquad s_{\pm x} = \min_{l=1,L_{\max}}\{(s_l)_{\pm x}\}, \tag{31e}$$

$$\chi_{\pm x} = \frac{(1+|\min(s_{\pm x},0)|)}{2}\min_{l=1,L_{\max}}\left\{|\max((s_l)_{\pm x},0)| + \frac{|(\phi_l)_{i,j}|}{|(\phi_l)_{i,j}|+|(\phi_l)_{i\pm1,j}|}|\min((s_l)_{\pm x},0)|\right\}. \tag{31f}$$

Note that cell face velocities are corrected independently:

$$\vec{u}_{i+1/2,j}^{n+1} = \vec{u}_{i+1/2,j}^{n} - \Delta t\left(\frac{\partial p^{n+1}}{\partial x}\right)_{i+1/2,j}. \tag{32}$$

The pressure gradient at the cell face is obtained based on straightforward central differences. The discrete correction expressions are similar to those given above.

5. Modeling the moving contact line

The precise relationship between contact line velocity and contact angle is poorly understood and most researchers have simplified this problem by employing experimentally measured contact angles as input boundary conditions for their numerical models. Pasandideh-Fard et al. [21] used the measured contact angle from photographs obtained from experiments as inputs to their numerical model. Fukai et al. [5] employed a similar approach in their study of wetting effects. Bussmann et al. [2] developed a model to evaluate contact angles as a function of contact line velocity. This model requires two inputs as well, the advancing and receding contact angles. Baer et al. [1] used a computationally tractable but simplified linear dependence of the contact angle on contact line velocity in their 3D finite-element moving mesh simulations. The model successfully accounted for the observed features of droplet spreading in 3D such as contact angle hysteresis and static contact angles. However, to ensure computational robustness for modeling wetting effects, a $\theta - u_c$ correlation is required to be applicable simultaneously to advancing and receding contact lines and over a large range of flow situations and geometry. Such a general relation is not available in the literature. In the following simulations, for modeling the contact angle depicted in Fig. 4(a), θ_{receding} and $\theta_{\text{advancing}}$ are assumed constant, as illustrated in Fig. 4(b). This is not a methodological limitation however and more sophisticated models for contact angle behavior, once established, can be easily included within the current framework.

Numerical modeling of fluid behavior in the vicinity of a moving contact line is complicated because the no-slip boundary condition at the solid–liquid interface leads to a force singularity at the contact line [10]. The problem can be resolved by replacing the no-slip boundary condition with a slip model [3]. Although this alleviates mathematical difficulties, there is no experimental evidence to determine which of the several available slip models is the most appropriate to use or whether physically such slip even occurs. In the present study, we simply apply the Navier slip boundary condition in the vicinity of the contact line. That is, we

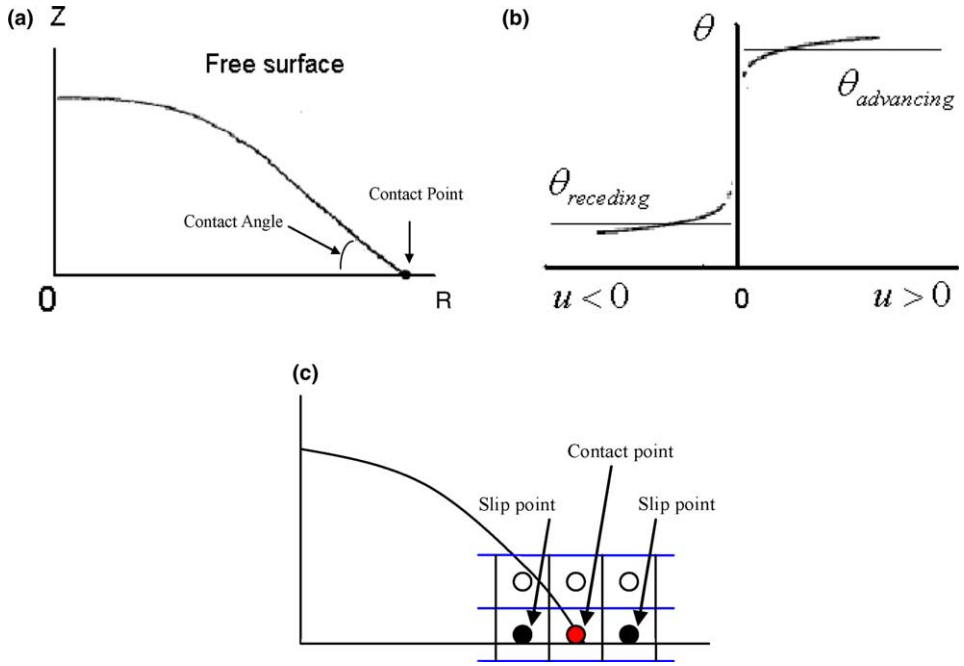

Fig. 4. (a) Axisymmetric droplet schematic and contact angle specification. (b) Illustration of model for the velocity dependent contact angle. (c) Illustration of implementation of slip boundary conditions for contact points.

allow the contact line to slip in a direction tangent to the substrate and thus alleviate the local singularity. In general form, the Navier slip boundary condition is: $\vec{\tau} = \frac{\mu}{l_s} u_{t_{\text{wall}}}$, where $\vec{\tau}$ is the tangential component of the surface traction vector, l_s is a slip length and the subscript t_{wall} indicates the value at the wall tangential to it. This is estimated in the current paper for an arbitrarily oriented solid surface from: $\mu \frac{\partial u_t}{\partial n} = \frac{\mu}{l_s} u_{t_{\text{wall}}}$, where n denotes the length increment in the normal direction to the surface and subscript t indicates the tangential wall component. By discretizing the normal gradient using a two-point discrete form and obtaining the value of velocity at the end of a normal projected [18] into the fluid from the contact point the value of $u_{t_{\text{wall}}}$ is obtained from the above slip condition. The slip length l_s was chosen to be Δx, the grid spacing [24]. The slip boundary condition is only applied to the fluid points which are in the immediate vicinity of the contact line. Fig. 4(c) illustrates the procedure for imposition of the slip boundary condition. First, a "contact point" is identified, which is the grid point in the spreading fluid that is immediately adjacent to the liquid–gas–solid tri-junction. Two other grid points that are the closest points to the identified contact point lying in the liquid and gas phases respectively are also identified. These three grid points in the fluid are given the Navier slip boundary condition on the wall, thus allowing the movement of the contact line. In the direction normal to the surface, the usual no-penetration boundary condition is employed at all solid-adjacent points.

6. Local level set reconstruction method for setting the contact angle

Fig. 5 illustrates the procedure employed to enforce the contact angle boundary condition on the solid surface. Fig. 5(a) shows the level set contour for a drop impacting on a solid surface in the

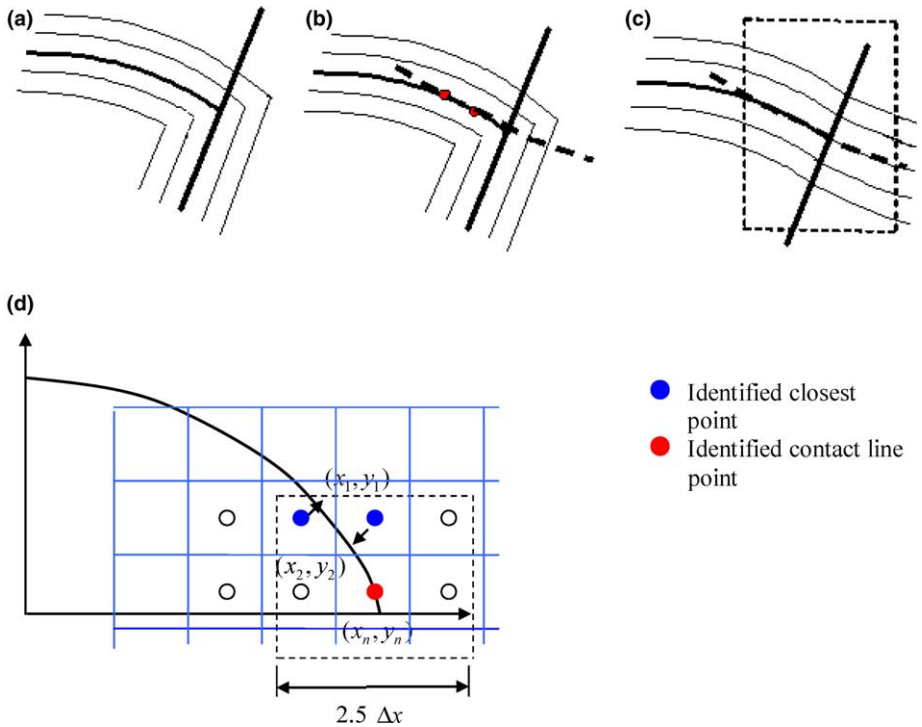

Fig. 5. Illustration of level set reconstruction and parabola fitting with a desired contact angle (92°). (a) Original level-set field. (b) Local parabola fitting. (c) Level-set field after reconstruction. (d) Illustration of parabolic curve fitting in level set field.

absence of a wetting model. When a contact angle condition is not imposed, the level-set field near the contact line is deformed to yield a flat droplet base that conforms to the solid surface due to the flow field that develops during the impact of the droplet on the solid surface. Obviously, the droplet does not have the desired contact angle near the contact line. Another problem with this level set field is that the sharp turn in the level set field will lead to an artificially large curvature which will distort the fluid flow. For comparison, Fig. 5(c) demonstrates the level set field after local reconstruction. In the vicinity of contact line, the local level set field is reconstructed in such a way that the specified contact angle is applied. This is achieved by fitting a parabolic curve that satisfies the contact angle condition at the solid surface while intersecting the solid surface at the contact line. The parabola is represented by the dotted line in Fig. 5(b). Fig. 5(d) shows how the curve fitting is implemented. First, the contact point is identified, as shown in Fig. 5(b); its coordinates are denoted as (x_0, y_0). Starting from this contact point all the fluid points within a box of side $2.5\Delta x$ are searched for two points in the spreading phase (liquid) that lie closest to the fluid–fluid interface (this is easily done using the distance function field). When those two points are identified, normals are projected to the interface to strike at points denoted as (x_1, y_1) and (x_2, y_2), respectively. This projection of the normal is straightforward in the level-set representation. For a grid point (i, j) in the liquid phase adjacent to the liquid–gas interface $\phi_{i,j} < 0$ and the normal intersects the interface at (x_1, y_1) and $\vec{x}_N = \vec{x}_{i,j} - \phi_{i,j}\vec{n}_{i,j}$ where $\vec{n}_{i,j}$ is the normal vector at point (i, j). In 2D these two points (x_1, y_1) and (x_2, y_2) plus the contact angle θ at the solid surface determine a unique parabola. The contact angle θ is the imposed spreading contact angle or the receding contact angle depending on the state of the contact line. The state of the contact line is determined by the contact line velocity u_c, which is the interpolated value of the fluid velocity in the vicinity of the contact point. As illustrated in Fig. 4(c), six points are used to interpolate the velocity field to obtain the contact line velocity u_c. Then, to apply the proper contact line condition:

1. First obtain u_c by interpolation. Also determine the angle made by the fluid–fluid interface with the solid–fluid interface at the contact point, $\theta = \cos^{-1}(\vec{n}_{FF} \cdot \vec{n}_{SF})$.
2. If $\theta_{receding} < \theta < \theta_{advancing}$, then apply $u_c = 0$. In this case, the contact angle is in hysteresis. Otherwise, if $u_c > 0$, then apply $\theta = \theta_{advancing}$ and if $u_c < 0$, then apply $\theta = \theta_{receding}$.

During hysteresis, the contact angle is not imposed and the current model allows the surface tension to retract the fluid back which decreases the angle from $\theta_{advancing}$ to $\theta_{receding}$. Implementation of the contact condition during hysteresis is different from that for the spreading and recoiling process in that during this stage the contact point is pinned, i.e. $u_c = 0$. To model the stationary contact line for this stage, the contact point coordinates (x_0, y_0) are saved right before hysteresis begins. In subsequent time steps, while the contact angle remains in the hysteretic range this fixed contact point (x_0, y_0) and the two points (x_1, y_1) and (x_2, y_2) obtained by normal projection (as described above) are used to determine a unique parabolic curve and the value of θ is allowed to float. In all these different fluid flow stages, the level set field in a box (of side length $4\Delta x$) surrounding the contact point is reassigned the value of the normal distance to this fitted parabolic curve. Then the entire level-set field is re-distanced to obtain a smooth level-set field that also satisfies the contact line conditions.

This is done for every time step and thus the contact angle is maintained as specified by the dynamic contact angle model. As can be seen from Fig. 5(c) the level set field close to the contact line is extended smoothly into the solid surface. This locally reconstructed level set field facilitates the local curvature calculation in the region adjacent to the contact line. We denote this extended level set field as ϕ' and the curvature is calculated based on this smoothed ϕ' field. Thus the curvature calculation does not see the highly curved level set field in Fig. 5(a).

7. Results

7.1. Droplet impact normal to a flat surface in the absence of a wetting model

Fig. 6 shows the impact, spreading and recoil behavior of a droplet impinging on a flat surface for the non-dimensional parameters $Re = 120$, $We = 80$, $Fr = 10^5$. To validate the calculations, the thickness (at the symmetry axis) of the spreading drop is plotted against time for different Reynolds numbers in

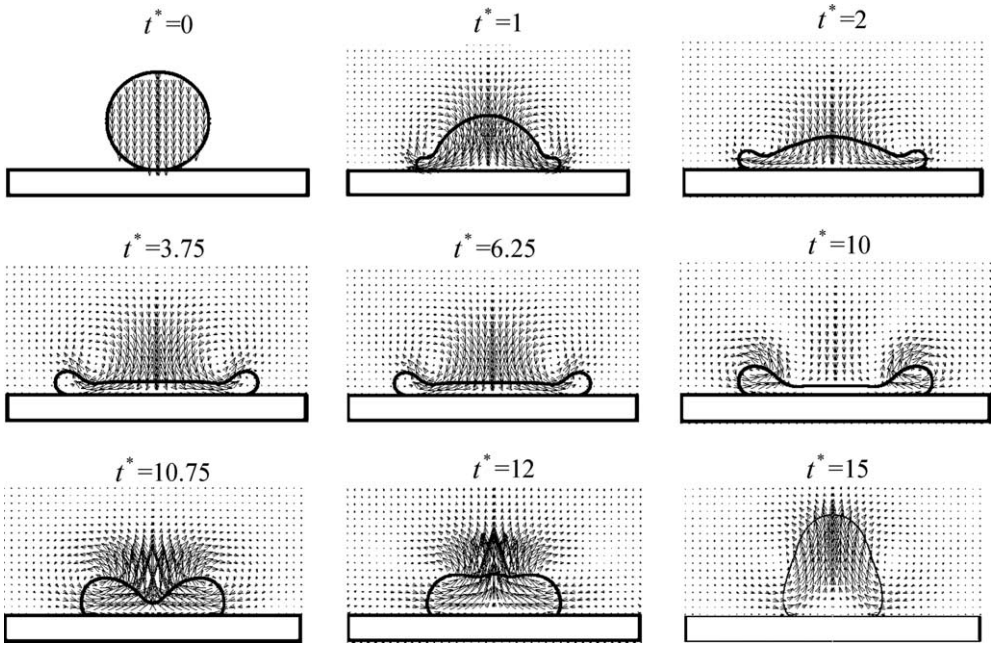

Fig. 6. Sequence of droplet shapes for normal impact on a solid plane surface impacting with parameters $Re = 120$, $We = 80$, $Fr = 10^5$.

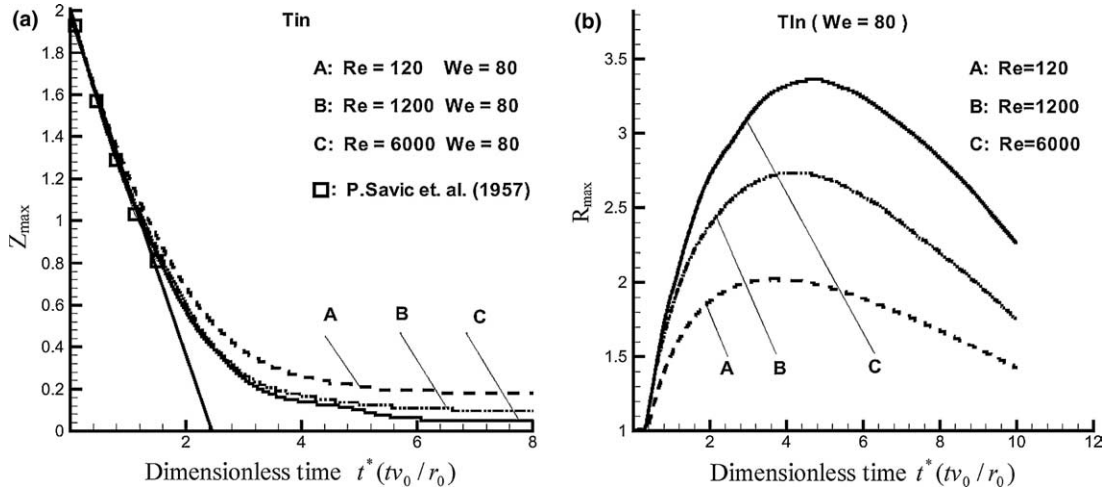

Fig. 7. (a) Effects of Reynolds number on the thickness of the droplet at the center of the axis of symmetry. (b) Spreading radius as a function of dimensionless time.

Fig. 7. The Weber number is held constant for these cases ($We = 80$). In Fig. 7(a), the results are compared with the experimental measurements carried out by Savic and Boult [25] using a high speed camera. The experiments were conducted with water droplets 4.8 mm in diameter, falling from a height of 1.83 m corresponding to $Re = 2.9 \times 10^4$. It is seen that very good agreement for the early stage of spreading is obtained with the present calculation. For the duration immediately after impact, the droplet motion is inertia dominated and is independent of viscous and capillary effects. This similarity in spreading lasts up to $t^* = 2$, demonstrating high rates of change in thickness independent of Reynolds number. Based on their analysis, Trapaga and Szekely [29] gave a linear relation between the impact velocity and dimensionless time for this very early stage of impact as $\frac{dh}{dt} = -c_o V_o$ {with c_o ranging from 0.7 to 0.84}. Based on the predictions of our numerical model, we obtain $\frac{dh}{dt} \approx 0.813$, which falls within the range given by Trapaga et al.

An important characteristic quantity in thermal spraying of metal droplets [7,8,19] is the final thickness at the center of the solidified splat. In an experimental study, [34] measured values of splat thickness for plasma-sprayed alumina powder with diameters ranging from 20 to 100 μm. It was found that the splat thickness is in the range of 2–4 μm. Trapaga and Szekely [29] suggest that the final thickness at the center is only a small fraction (5%) of the initial droplet diameter. The final thickness obtained in the current simulations range from 4% to 15%. Fukai et al. [6] found that their calculated final splat thickness is around 10% of the pre-impact droplet radius. While in our predictions, for Reynolds number of 1200 and 6000, the predicted results are in very good agreement with above reference values (≅5%), the result (≅14%) for small Reynolds number ($Re = 120$) is slightly above the suggested value of 10% by Fukai et al. [6]. Another characteristic trend observed is that the final splat thickness is dependent on Reynolds numbers, with larger Reynolds numbers tending to have smaller maximum thickness as expected. This is clearly demonstrated in Fig. 7(b) and is consistent with the observations of Fukai et al. [5] and Trapaga and Szekely [29]. This phenomenon is also consistent with the notion that higher Reynolds numbers should correspond to larger maximum spreading radii, as shown in Fig. 7(b).

7.2. Droplet impact on arbitrarily shaped solid surfaces

Simulations of impact of droplets on solid surfaces of arbitrary shape are relatively sparse in the literature. Of the available simulations [2,23] none are sharp-interface models for the fluid–fluid interface and the solid–fluid interface is typically treated in a simplistic manner by using a volume-fraction solid

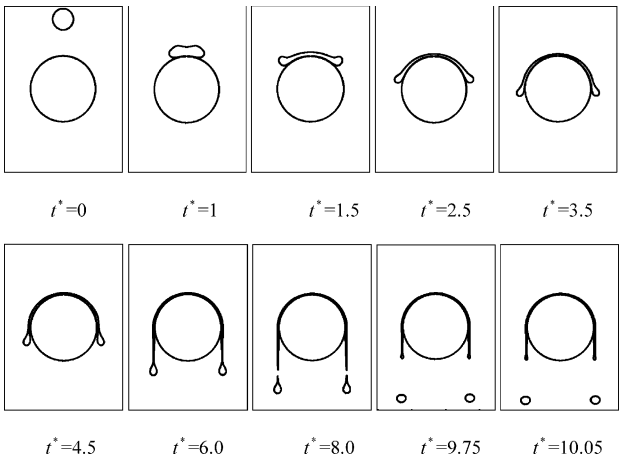

Fig. 8. Shapes of a droplet impacting on a cylinder ($Re = 10$, $We = 333$). The formation of a filament on each side is seen along with the detachment of a pendant drop and formation of a secondary pendant drop after retraction of the remaining filament.

approach or a stair-step geometry aligned with the Cartesian mesh. The methodology developed in this paper allows for the calculation of impact on arbitrarily shaped solid objects, without these limitations of previous methods. By using the general form of the discretization scheme shown in Eq. (25) independently along each coordinate direction, the treatment of impact on curved surfaces is no different from that on a plane surface. Here we demonstrate the capability of the method to solve the impact problem without involving the issue of contact line dynamics. Results with wetting effects are presented in a subsequent section.

The first calculation carried out is for a water droplet suspended in air which impacts on a stationary solid cylindrical surface. The following dimensionless parameters apply: $Re = 10$, $We = 10$, $\frac{\rho_{\text{liquid}}}{\rho_{\text{gas}}} = 100$, $Fr = 1$. The liquid droplet starts to move down due to gravity, impacts on the curved surface, spreads and drips down, as observed in Fig. 8. Eventually, this droplet undergoes severe deformation following which the droplet breaks and forms two smaller drops that fall under gravity. The falling film of fluid then retracts due to capillary forces and accumulates to form a second drop, which in turn is pulled down due to gravity and breaks away from the main drop.

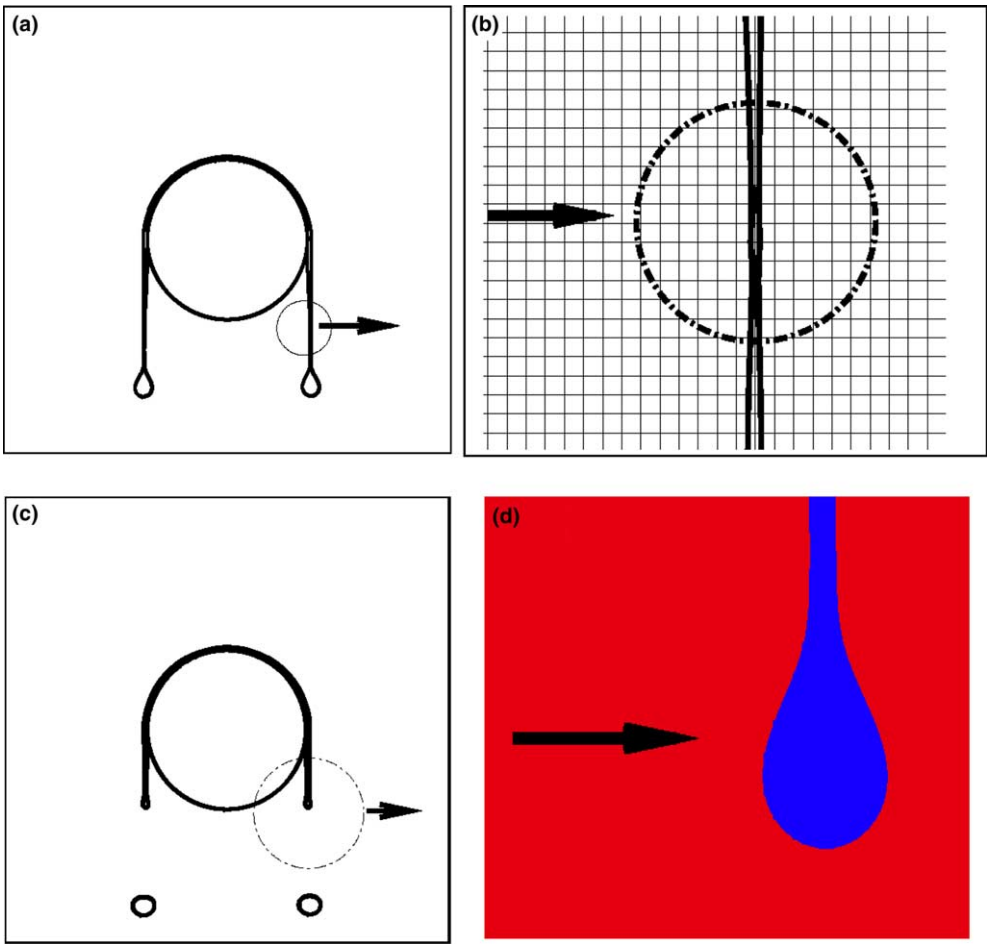

Fig. 9. (a) Droplet shape close to the breaking time of the filament. (b) Closer examination of the filament near the breaking time. The grid is shown as background. (c) Formation of the second pendant drop after retraction of the filament following detachment of the first pendant drop. (d) Closer view of the second pendant drop.

To demonstrate the ability of the method to capture the interface sharply, it is useful to amplify further the features observed in Fig. 8. As illustrated in Fig. 9(a), two very thin filaments are formed on the two sides of the spreading droplet which eventually result in drops. Amplifying this thin filament, as shown in Fig. 9(b), it is observed that the entire filament lies within two mesh widths. The detail of the secondary drop formed after the film of fluid retracts following detachment of the first breakaway satellite drop is also shown in Fig. 9(c) and (d). The present sharp interface method can handle these rather fine structures robustly and can also compute through topological changes without difficulty. Note that the calculations were performed in a two-dimensional system without imposing symmetry, i.e. the entire cylinder and drop was computed. The method preserves very well the symmetry of the evolution of the fluid–fluid boundary.

In the second example shown in Fig. 10, the solid surface on which the droplet impacts is an inclined plane, and the non-dimensional parameters are: $Re = 50$, $We = 333.3$, $\frac{\rho_{\text{liquid}}}{\rho_{\text{gas}}} = 1000$, $Fr = 1$. As shown in the sequential frames in Fig. 10, the droplet is driven toward the plate by gravity and then undergoes impact and spreading on the inclined surface. Eventually, the mass accumulation on the lower end of the droplet results in a drop which drips down the inclined surface. There is also a drop that forms on the upper end of the main drop, which flows over the edge of the plane and breaks into a second detached drop. However, the second detached drop does not drip away from the surface but instead is arrested by viscosity and remains adhered to the wall. Thus, the interface interaction algorithm can track multiple, disconnected pockets of fluid and their dynamics on the solid surface without requiring any intervention or complicated mesh management strategies.

7.3. Wetting and spreading

7.3.1. Water droplet impact on a flat surface

Droplet impact on a solid surface is simulated for the conditions in [5], corresponding to $Re = 3130$, $We = 64$. Advancing and receding contact angles are specified to be 92° and 60°, respectively. The sequence of deformation of the droplet is shown in Fig. 11. For clear comparison, the computed drop shapes are plotted together with those reported by Fukai et al. [5] corresponding to the same instant of time are plotted. The present calculated results are shown to the left of the axis and Fukai et al.'s results are shown to the

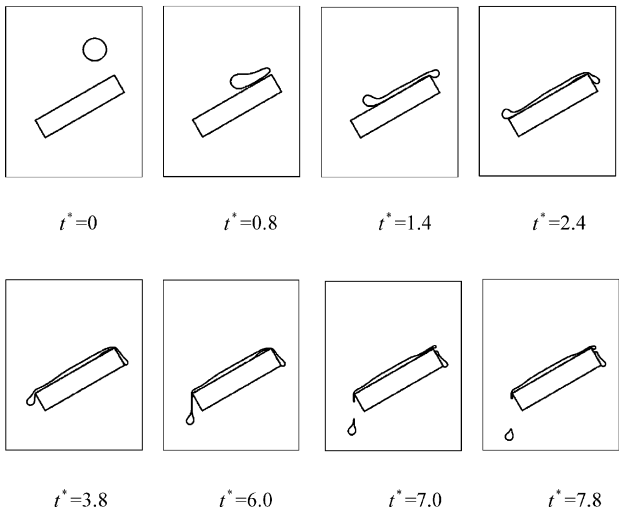

Fig. 10. The evolution of a droplet after impact with an inclined plane. The parameters as $Re = 50$, $We = 333$, density of liquid is 1000 times that of the surrounding gas.

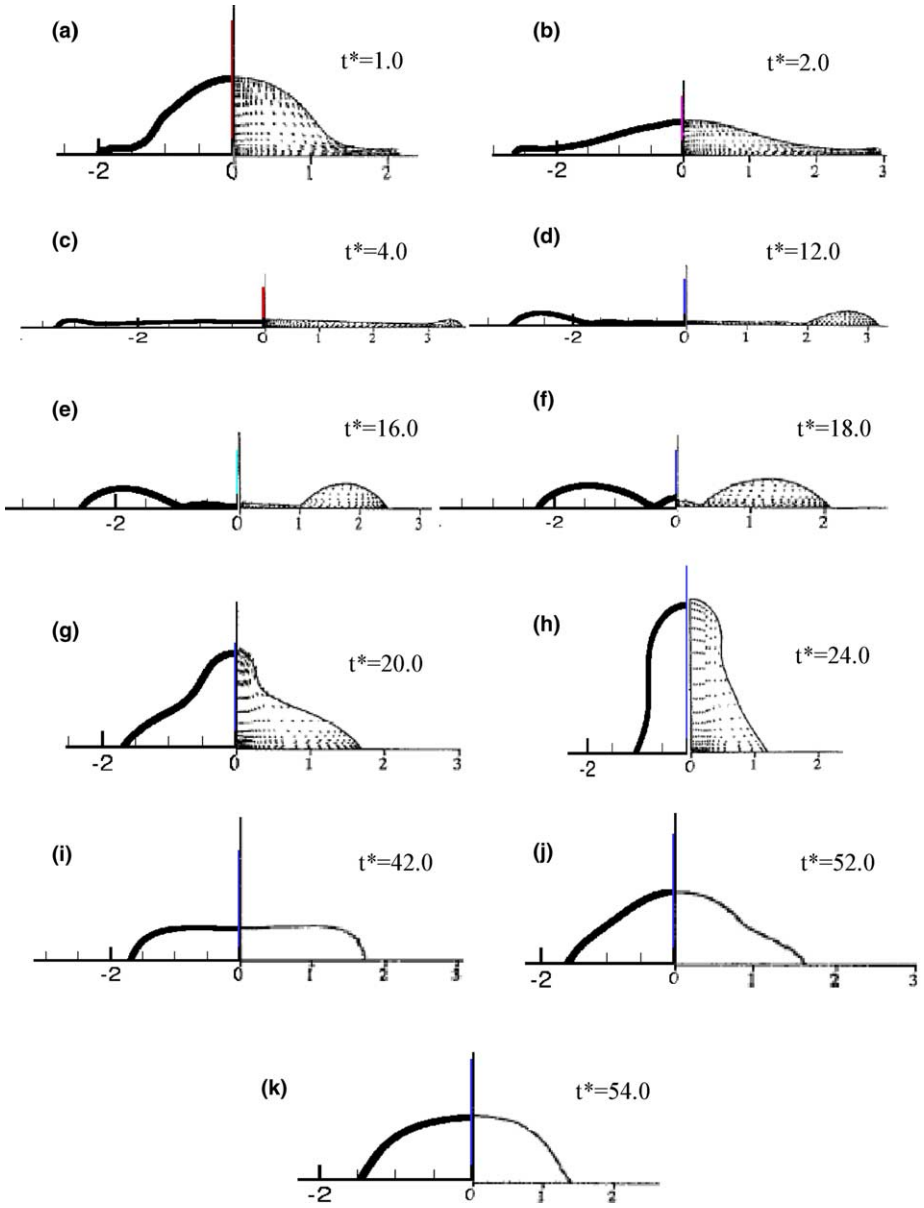

Fig. 11. Calculated droplet spreading shapes compared with numerical results from Fukai et al. (1996) for droplet impact with $Re = 3010$, $We = 57$, $\theta_{\text{advancing}} = 92°$, $\theta_{\text{receding}} = 60°$, $\theta_{\text{static}} = 75°$.

right. It is observed that a thin film is formed around the droplet right after the impact. Consistent with Fukai's prediction, the spreading process ends at $t^* = 7.5$. During this spreading process, the contact angle (see Fig. 11(c)) is maintained at the advancing value of 92° as specified by the model. Contact angle hysteresis takes place approximately from $t^* = 5.0$ to $t^* = 7.0$. After $t^* = 7.5$, the recoil process begins and the fluid recedes from the maximum wetted radius at the specified receding contact angle. A bulk upward

motion near the axis occurs after $t^* = 28$ and oscillation of the droplet ensues after this time. Equilibrium is achieved after a few oscillations. The equilibrium shape of the drop is characterized by a typical sessile spherical cap drop shape with an equilibrium angle of 75°. This angle has a value between the advancing and receding contact angle.

The above simulation successfully captures all the essential features of droplet impact. From Fig. 11, it can be seen that very close match is obtained with the results from [5] in terms of drop shapes and timing of all the characteristic processes. However, some differences in the predictions of the maximum spreading radius and droplet thickness are observed. The maximum spreading radius reported by Fukai et al. in this case is 3.6; the current predicted result is 3.45. This difference is also reflected as a discrepancy in the maximum drop thicknesses. The current model obtains 2.35 while Fukai et al. reported a value of 2.7. These differences can be better seen in Fig. 12, in which the current computed spreading radius (Fig. 12(a)) as well as the droplet thickness (Fig. 12(b)) are compared with the experimental results provided by Fukai et al. However, the time for the droplet to reach maximum spreading from our calculation is 4.2, which is in excellent agreement with that reported by Fukai et al. The match in time can also be seen by comparing subsequent hysteresis and spreading and recoil processes.

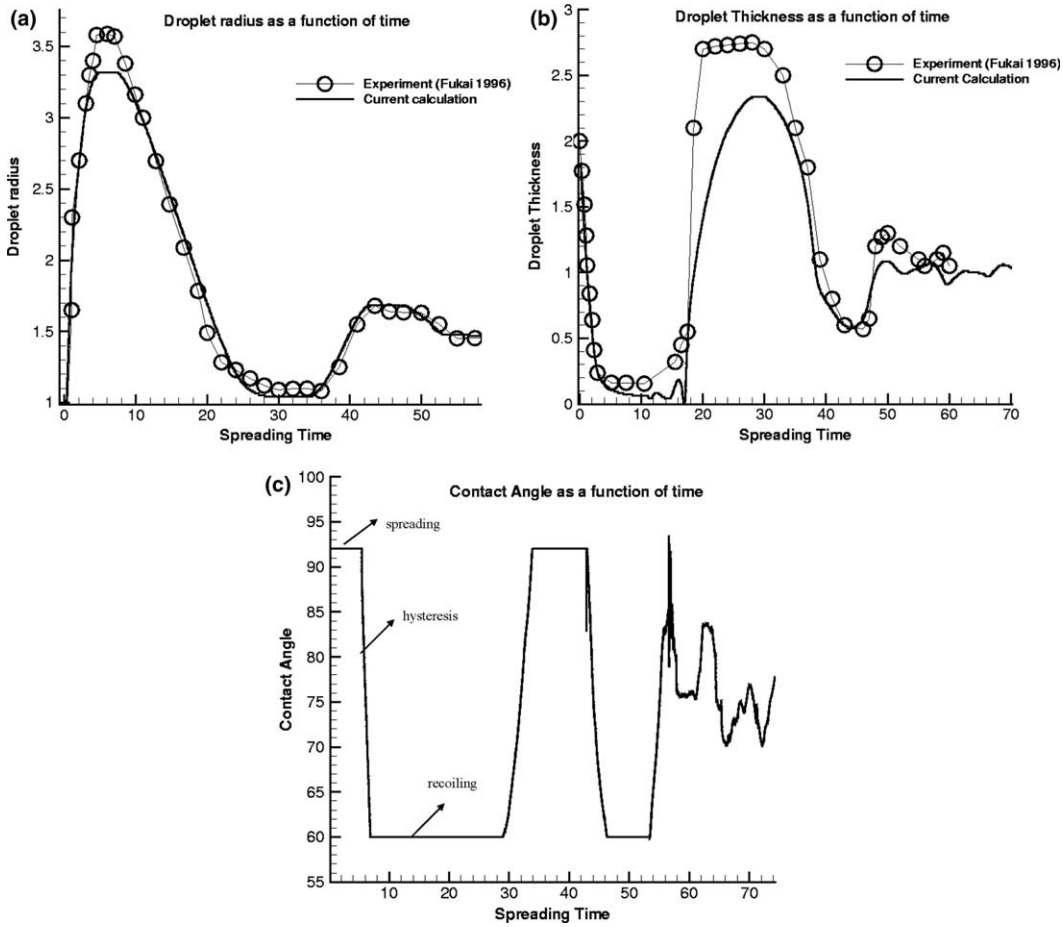

Fig. 12. Quantitative results for $Re = 3010$, $We = 57$, $\theta_{\text{advancing}} = 92°$, $\theta_{\text{receding}} = 60°$, $\theta_{\text{static}} = 75°$. (a) Calculated droplet spreading radius compared with experimental results. (b) Calculated droplet thickness compared with experimental results. (c) Contact angle for water droplet.

Fig. 12(c) depicts the contact angle as a function of time. As observed from this figure, if the droplet is spreading, a pre-specified constant advancing contact angle (92°) is imposed. If the droplet undergoes recoiling, a specified constant receding contact angle (60°) is imposed. During hysteresis, no fixed contact angle is imposed but the contact angle is free to be adjusted by surface tension while the contact line remains motionless.

7.3.2. Impact of droplets on arbitrarily shaped solid surfaces

Fig. 13 shows a two-dimensional planar simulation of droplet impact on a solid surface inclined at 45° to the horizontal. The non-dimensional parameters are: $Re = 3333$, $We = 100$, $\frac{\rho_{\text{liquid}}}{\rho_{\text{gas}}} = 1000$. The water droplet

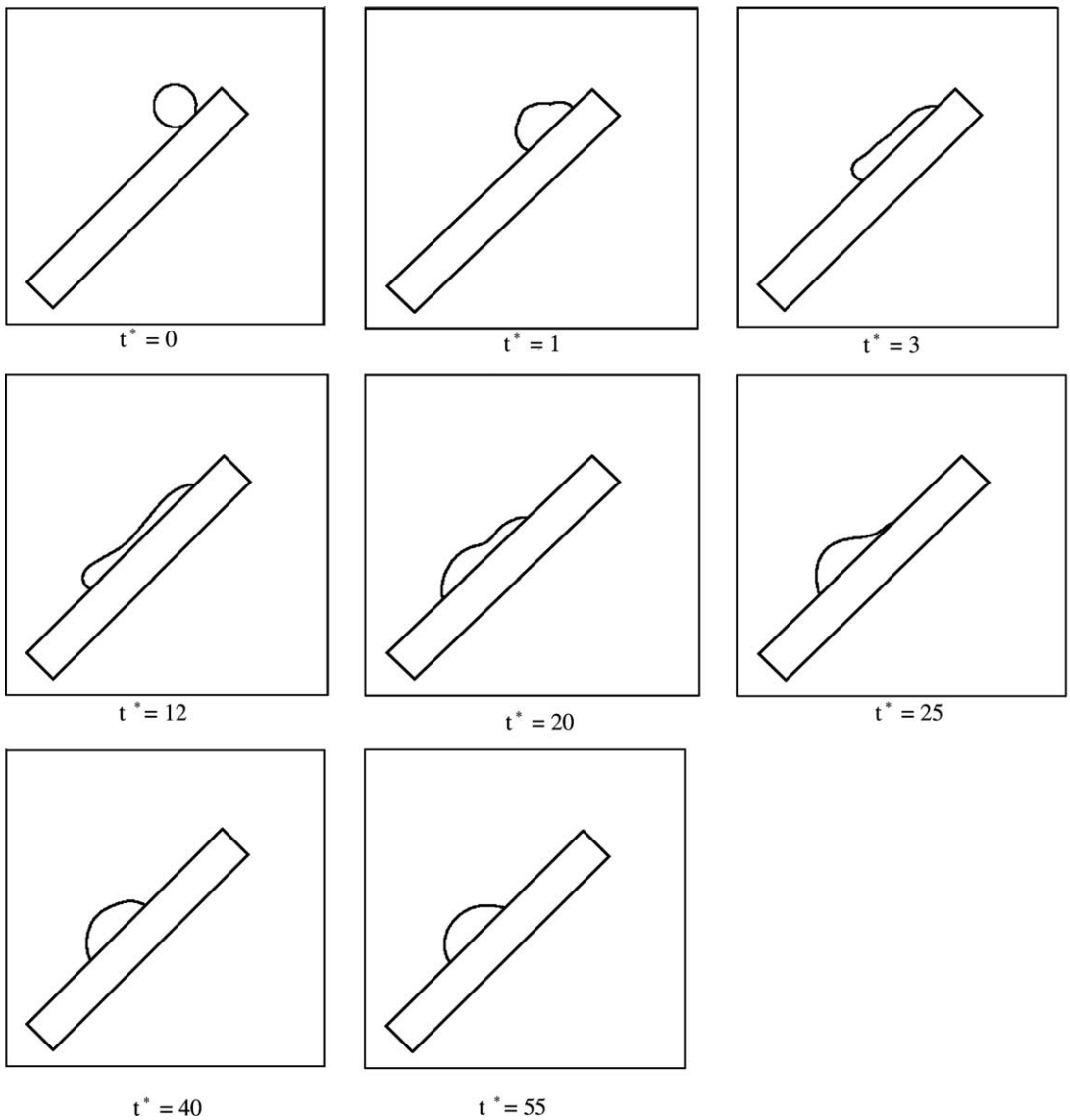

Fig. 13. Calculated shapes for water droplet impacting on inclined surface with $Re = 3333$, $We = 100$, $\theta_{\text{advancing}} = 110°$, $\theta_{\text{receding}} = 60°$.

is given an initial dimensionless impact velocity of 1. Apart from the fact that the solid geometry immersed in the Cartesian mesh is not coincident with the coordinate directions, this case also differs from the previous cases in that there are two contact lines in this impact scenario. These two contact lines move with different velocities and thus are represented by different contact angles. One can clearly identify two

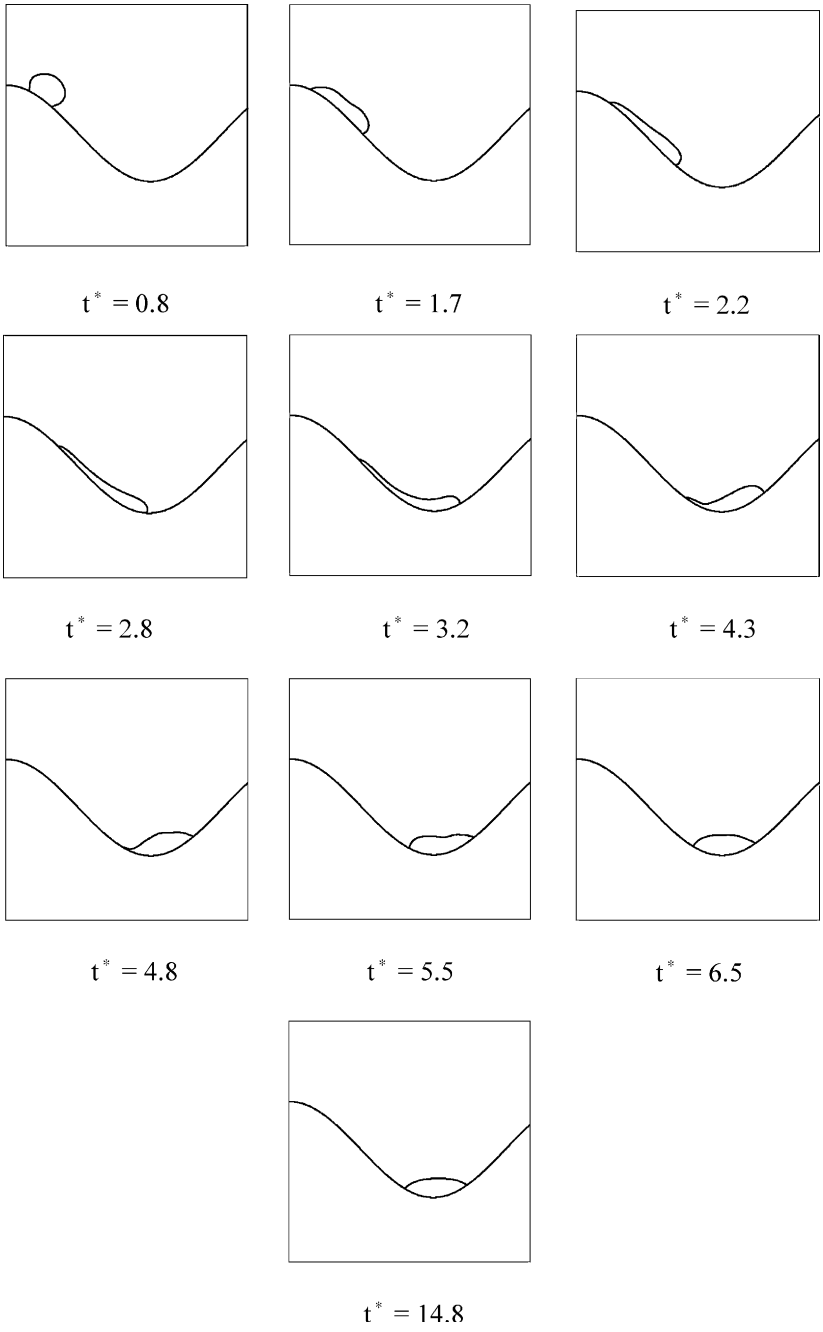

Fig. 14. Calculated shapes for water droplet impacting on curved surface with $Re = 3333$, $We = 50$, $\theta_{\text{advancing}} = 110°$, $\theta_{\text{receding}} = 60°$.

distinctive contact angles when the droplet is sliding down the curved surface, the one to the left is the advancing (110°) and on the right is the receding (60°) contact angle. The droplet undergoes spreading, hysteresis, recoiling, as well as subsequent oscillations as it slides down the plane. It eventually reaches a static shape represented by two distinctive static contact angles. The upper contact line has an angle 69° and the lower contact angle is 72°. An experimental study of droplet impact on an inclined surface can be found in Kang et al. (2000) [13]. Their study included heat transfer and its effects on the droplet spreading. The droplet shapes obtained in the above simulation are qualitatively similar to those in the experiments for similar parameter values. Bussmann et al. [2] numerically modeled three-dimensional droplet impact on an inclined surface using a VOF representation for the fluid and a volume-fraction approach for the solid. Droplet shapes and spreading behavior similar to those seen in the present 2D simulations were observed, both in terms of the droplet shapes as well as the final displacement and resting shape.

To demonstrate that droplet impact with wetting effects can be simulated on an arbitrary-shaped surface, impact onto a shape like a sinusoid shaped solid surface is shown in Fig. 14. The key parameters are: $Re = 3333$, $We = 50$, $\frac{\rho_{\text{liquid}}}{\rho_{\text{gas}}} = 1000$, $\theta_{\text{advancing}} = 110°$, $\theta_{\text{receding}} = 60°$. The sequence of deformation of the droplet is depicted in the figure. The droplet is seen to flow down the surface to the trough, with the specified receding and advancing contact angles. It overshoots the trough due to inertia but finally settles to equilibrium in the trough with the resting contact angle values of 88.3° and 86.5° at the two contact lines.

8. Summary

A sharp-interface method is presented in this paper for the simulation of fluid–fluid interfaces interacting with solid–fluid interfaces. The specific problem of impact of droplets with surfaces of arbitrary shape is chosen to demonstrate the technique. The framework of the method rests on a level-set representation of all interfaces. This allows for easy implementation of a finite-difference scheme to discretize the governing equations in the presence of interfaces in such a way that explicit knowledge of the interface location is not necessary. The implicit embedded interface derived from the level-set field suffices to provide a sharp description of the interface and to apply the necessary boundary conditions and jump conditions on the interfaces. The discretization scheme unifies a sharp-interface solid–fluid interface treatment presented in [18] with the ghost-fluid method. One crucial aspect of multiphase interactions is the wetting of the solid surface by the fluid and the dynamics of the three-phase contact line. The model to include this dynamics on an arbitrarily shaped solid has been advanced in this paper within the framework of a sharp-interface approach.

The method has been used to study the impact of droplets in several scenarios and a range of parameters has been covered. The results are shown to match other numerical and experimental results well in the range of parameters explored. This includes problems where the contact line dynamics is important. Benchmark results for the impact and spreading of droplets on arbitrary surfaces are lacking. In such cases, the method is shown to provide qualitatively correct solutions. Study of the three-dimensional droplet-surface interaction problem is now in progress.

Acknowledgments

This work was performed with support from the Computational Mechanics Branch, AFRL-MNAC, Eglin, FL (Project manager Mr. Joel Stewart) and AFOSR Computational Mathematics Division (Program manager Dr. Fariba Fahroo).

References

[1] T.A. Baer, R.A. Cairncross, P.R. Schunk, R.R. Rao, P.A. Sackinger, A finite element method for free surface flows of incompressible fluids in three dimensions. Part II: Dynamic wetting lines, International Journal for Numerical Methods in Fluids 33 (3) (2000) 405.

[2] M. Bussmann, J. Mostaghimi, S. Chandra, On a three-dimensional volume tracking model of droplet impact, Physics of Fluids 11 (6) (1999) 1406–1417.

[3] E.B. Dussan, E. Rame, S. Garoff, On identifying the appropriate boundary-conditions at a moving contact line – an experimental investigation, Journal of Fluid Mechanics 230 (1991) 97–116.

[4] R. Fedkiw, X.-D. Liu, The ghost fluid method for viscous flows, in: M. Hafez, J.-J. Chattot (Eds.), Innovative Methods for Numerical Solutions of Partial Differential Equations, World Scientific Publishing, New Jersey, 2002, pp. 111–143.

[5] J. Fukai, Y. Shiiba, T. Yamamoto, O. Miyatake, D. Poulikakos, C.M. Megaridis, Z. Zhao, Wetting effects on the spreading of a liquid droplet colliding with a flat surface – experiment and modeling, Physics of Fluids 7 (2) (1995) 236–247.

[6] J. Fukai, Z. Zhao, D. Poulikakos, C.M. Megaridis, O. Miyatake, Modeling of the deformation of a liquid droplet impinging upon a flat surface, Physics of Fluids A – Fluid Dynamics 5 (11) (1993) 2588–2599.

[7] R. Ghafouri-Azar, S. Shakeri, S. Chandra, J. Mostaghimi, Interactions between molten metal droplets impinging on a solid surface, International Journal of Heat and Mass Transfer 46 (8) (2003) 1395–1407.

[8] E. Gutierrezmiravete, E.J. Lavernia, G.M. Trapaga, J. Szekely, N.J. Grant, A mathematical-model of the spray deposition process, Metallurgical Transactions A – Physical Metallurgy and Materials Science 20 (1) (1989) 71–85.

[9] F.H. Harlow, J.P. Shannon, The splash of liquid droplet, Journal of Applied Physics 38 (1967) 3885.

[10] L.M. Hocking, Rival contact-angle models and the spreading of drops, Journal of Fluid Mechanics 239 (1992) 671–681.

[11] D. Jacqmin, An energy approach to the continuum surface method, in: 34th Aerospace Science Meeting, No. AIAA-96-0858, 1996.

[12] M. Kang, R.P. Fedkiw, A boundary condition capturing method for multiphase incompressible flow, Journal of Scientific Computing 15 (2002) 323–360.

[13] B.S. Kang, D.H. Lee, On the dynamic behavior of a liquid droplet impacting upon an inclined heated surface, Experiments in Fluids 29 (4) (2000) 380–387.

[14] D.B. Kothe, R.C. Mjolsness, M.D. Torrey, Ripple: A computer program for incompressible flows with free surfaces, Technical Report LA-12007-MS, 1991.

[15] Z.L. Li, M.C. Lai, The immersed interface method for the Navier–Stokes equations with singular forces, Journal of Computational Physics 171 (2) (2001) 822–842.

[16] X.D. Liu, R.P. Fedkiw, M.J. Kang, A boundary condition capturing method for Poisson's equation on irregular domains, Journal of Computational Physics 160 (1) (2000) 151–178.

[17] Liu, Huimin, Enrique J. Lavernia, Roger H. Rangel, Numerical simulation of substrate impact and freezing of droplets in plasma spray processes, Journal of Physics D: Applied Physics 26 (11) (1993) 1900–1908.

[18] S. Marella, S. Krishnan, H. Liu, H.S. Udaykumar, Sharp interface Cartesian grid method I: an easily implemented technique for 3D moving boundary computations, Journal of Computational Physics (accepted).

[19] J. Mostaghimi, M. Pasandideh-Fard, S. Chandra, Dynamics of splat formation in plasma spray coating process, Plasma Chemistry and Plasma Processing 22 (1) (2002) 59–84.

[20] D.R. Noble, T.A. Baer, R.R. Rao, Contact angle specification in level-set simulations, Sandia National Laboratories Internal Report, 1994; Obtained by private communication with D.R. Noble.

[21] M. Pasandideh-Fard, Y.M. Qiao, S. Chandra, J. Mostaghimi, Effect of surface tension and contact angle on the spreading of a droplet impacting on a substrate, American Society of Mechanical Engineers, Fluids Engineering Division (Publication) FED, Experimental and Numerical Flow Visualization 218 (1995) 53–61.

[22] M. Pasandideh-Fard, R. Bhola, S. Chandra, J. Mostaghimi, Deposition of till droplets on a steel plate: simulations and experiments, International Journal of Heat and Mass Transfer 41 (19) (1998) 2929–2945.

[23] M. Pasandideh-Fard, M. Bussmann, S. Chandra, J. Mostaghimi, Simulating droplet impact on a substrate of arbitrary shape, Atomization and Sprays 11 (4) (2001) 397–414.

[24] M. Renardy, Y. Renardy, J. Li, Numerical simulation of moving contact line problems using a volume-of-fluid method, Journal of Computational Physics 171 (1) (2001) 243–263.

[25] P. Savic, G.T. Boult, The fluid flow associated with the impact of liquid drops with solid surfaces, in: Proceedings of the Heat Transfer Fluid Mechanics Institute, 1957.

[26] K.A. Smith, F.J. Solis, D.L. Chopp, A projection method for motion of triple junctions by level sets, Interfaces and Free Boundaries 4 (3) (2002) 263–276.

[27] M. Sussman, An adaptive mesh algorithm for free surface flows in general geometries, in: Adaptive Method of Lines, Chapman-Hill/CRC Press, Boca Raton, FL, 2001, pp. 207–227.

[28] G. Trapaga, E.F. Matthys, J.J. Valencia, J. Szekely, Fluid-flow, heat-transfer, and solidification of molten-metal droplets impinging on substrates – comparison of numerical and experimental results, Metallurgical Transactions B – Process Metallurgy 23 (6) (1992) 701–718.
[29] G. Trapaga, J. Szekely, Mathematical-modeling of the isothermal impingement of liquid droplets in spraying processes, Metallurgical Transactions B – Process Metallurgy 22 (6) (1991) 901–914.
[30] K. Tsurutani, M. Yao, J. Senda, H. Fujimoto, Numerical-analysis of the deformation process of a droplet impinging upon a wall, JSME International Journal Series II – Fluids Engineering Heat Transfer Power Combustion Thermophysical Properties 33 (3) (1990) 555–561.
[31] T. Ye, R. Mittal, H.S. Udaykumar, W. Shyy, An accurate Cartesian grid method for viscous incompressible flows with complex immersed boundaries, Journal of Computational Physics 156 (2) (1999) 209–240.
[32] H.K. Zhao, B. Merriman, S. Osher, L. Wang, Capturing the behavior of bubbles and drops using the variational level set approach, Journal of Computational Physics 143 (2) (1998) 495–518.
[33] L.L. Zheng, H. Zhang, An adaptive levelset method for moving-boundary problems: application to droplet spreading and solidification, Numerical Heat Transfer Part B – Fundamentals 37 (2000) 437–454.
[34] P. Zoltowski, Les couches en alumine effectuees au pistolet a plasma (Plasma gun spraying of aluminum oxide – 1), Revue Internationale des Hautes Temperatures et des Refractaires 5 (4) (1968) 253–265 (in French).